Journal of Applied Electrochemistry (2026) 56:34
https://doi.org/10.1007/s10800-025-02389-9

RESEARCH ARTICLE

# Electrochemical nitrate sensing based on reduced graphene oxide/conducting polyaniline nanocomposite in environmental water sources

**Siti Nur Akmar Mohd Yazid[1,2] · Mohamad Idris Saidin[1,2] · Illyas Md Isa[1,2] · Chin Suk Fun[3] · Ain Nadirah Romainor[3] · Nur Indah Wardani[4] · Mohamad Syahrizal Ahmad[1,2]**

Received: 17 September 2025 / Accepted: 8 December 2025


## Abstract

In this study, a novel non-enzymatic electrochemical sensor based on a nanocomposite of reduced graphene oxide and conducting polyaniline, denoted as reduced graphene oxide/polyaniline/glassy carbon electrode (rGO/PANI/GCE), was developed for detecting nitrate ions in environmental water sources. The reduced graphene oxide/polyaniline nanocomposite was synthesised by dispersing graphene oxide in water to form a homogeneous suspension, preparing polyaniline separately through chemical oxidative polymerisation, and subsequently combining them while reducing graphene oxide to reduced graphene oxide to produce a uniform composite material. The reduced graphene oxide/polyaniline nanocomposites were deposited on a glassy carbon electrode and applied as the working electrode. The nanocomposite was characterised using Fourier-transform infrared spectroscopy, field-emission scanning electron microscopy, energy-dispersive X-ray spectroscopy, and X-ray diffraction. Cyclic voltammetry, electrochemical impedance spectroscopy, and square wave voltammetry were employed to evaluate the electrochemical behaviour of the sensor. The reduced graphene oxide/polyaniline/glassy carbon electrode exhibited electrocatalytic oxidation performance that surpassed those of the polyaniline/glassy carbon electrode, the graphene oxide/glassy carbon electrode, and the bare glassy carbon electrode. Under optimal conditions, the recorded current showed a linear correlation with nitrate ion concentration in the range of 7 to 45 µM. The regression equation was $I = 22.943 + 0.863$ C ($R^2 = 0.982$). The sensor demonstrated a sensitivity of 0.863 µA $\mu M^{-1}$ with a detection limit of 1.74 µM. It also exhibited reproducibility with a relative standard deviation of 2.99% for nitrate ion detection. Recovery studies were conducted to assess the practical applicability of the sensor, yielding recovery rates between 95% and 105% for spiked samples. The sensor performed effectively with real water samples, demonstrating its suitability for reliable water quality monitoring.

✉ Siti Nur Akmar Mohd Yazid
snakmar@fsmt.upsi.edu.my

[1] Department of Chemistry, Faculty of Science and Mathematics, Universiti Pendidikan Sultan Idris, Tanjong Malim, Perak, Malaysia

[2] Nanotechnology Research Centre, Faculty of Science and Mathematics, Universiti Pendidikan Sultan Idris, Tanjong Malim, Perak, Malaysia

[3] Department of Chemistry, Faculty of Resource Science and Technology, Universiti Malaysia Sarawak, Kota Samarahan, Sarawak, Malaysia

[4] Department of Environmental Engineering Pollution Control, Politeknik Negeri Cilacap, Kabupaten Cilacap, Central Java, Indonesia

Published online: 14 January 2026

**Graphical abstract**

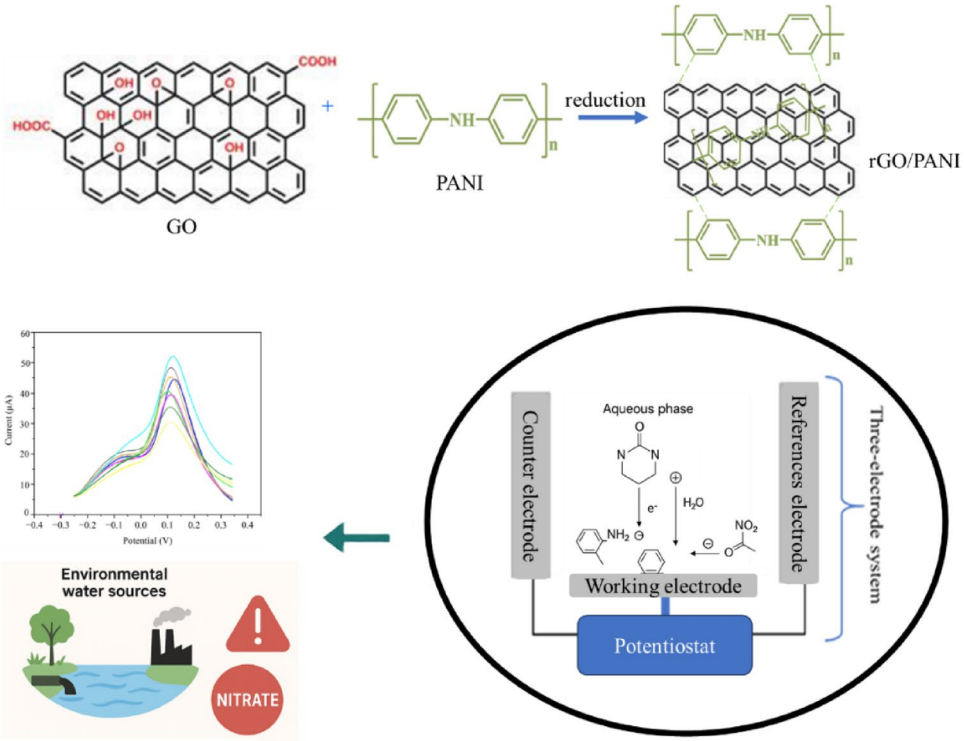


**Keywords** Environmental water analysis · Glassy carbon electrode · Nitrate sensing · Polyaniline nanocomposite · Reduced graphene oxide

## 1 Introduction

The rise in the amount of nitrate ions ($NO_3^-$) in aqueous systems has become a major environmental issue, primarily due to the excessive use of nitrogenous fertilisers in farming, industrial effluents, and poor handling of organic and chemical waste [1]. A high concentration of $NO_3^-$ in water bodies poses significant risks to both the environment and human health. The excess of $NO_3^-$ causes eutrophication of aquatic environments, facilitating excessive algal growth, depleting oxygen, and ultimately leading to biodiversity depletion in marine environments [2, 3]. This pressing the urgent need for reliable, practical, and cost-effective strategies to monitor $NO_3^-$ contamination. While conventional techniques such as UV–visible spectrophotometry [4], ion chromatography [5], and colourimetric assays [6] deliver high precision and accuracy in laboratory settings, they remain costly, time-consuming, and unsuitable for real-time or on-site water monitoring. The introduction of new electrochemical sensing methods could make it possible to evaluate $NO_3^-$ more reliably and more competitively. These sensors are being developed based on the principle of transducing chemical information, such as the redox behaviour of $NO_3^-$ at the electrode surface, and converting the information into measurable electrical signals [7]. The advantages of electrochemical sensors include high sensitivity, which enables the detection of $NO_3^-$ at extremely low concentrations, as well as being cost-effective and portable [8, 9]. Their performance depends strongly on the electrode material as it serves as the point of contact that connects the sensor to the analyte through the transfer of electrons [10]. In this context advanced nanomaterials including carbon-based nanostructures and conducting polymers have shown impressive potential.

Accordingly, graphene, widely used as reduced graphene oxide (rGO), is a vital electrode material that greatly improves the performance of electrochemical sensors. rGO has a large specific surface area (2630 $m^2\ g^{-1}$), excellent chemical stability, a broad potential range, and fast electron mobility, which together enable quick electron transport, high current response, and structural stability. Moreover, the two-dimensional planar structure allows its surface to be easily modified, functionalised, and combined into composites [11, 12]. However, despite these benefits, rGO often displays limited redox activity and lacks abundant surface functional groups necessary for specific interactions with

analytes [13]. Additionally, rGO sheets tend to agglomerate due to π–π stacking and van der Waals forces, leading to a decreased effective surface area and reduced electrochemical activity [14]. To overcome these challenges, researchers are increasingly developing rGO-based composites with conducting polymers (CPs) to utilise the strong synergy between the two materials. CPs possess unique properties, such as optical, electrical, and mechanical features, comparable to those of semiconductors and metals. Furthermore, they are cost-effective and environmentally friendly, broadening their range of applications [15, 16].

Polyaniline (PANI) is one of the most essential CPs because of its stability in air and moisture, in both doped (conducting) and dedoped (insulating) forms. PANI is commonly synthesised on various substrates via chemical oxidative polymerisation, in which oxidant-activated aniline monomers couple to form higher-molecular-weight chains [17]. PANI exists primarily as leucoemeraldine (LE) (fully reduced), emeraldine base (EB) (oxidised halfway), and pernigraniline (PE) (fully oxidised). LE and PE are both nearly insulating in nature due to the insufficient delocalized charge carriers in LE and over-oxidation in PE, which critically hinders charge transport. In contrast, the intermediate form, the EB, is the most stable and protonated. It is highly conductive as a result of polarons and bipolarons formed on the conjugated backbone [18, 19]. In electrochemical sensing, this redox tunability is a significant advantage as the electrode's electrical and chemical properties can be switched or optimised simply by adjusting the doping state of PANI. The polymer also offers a high surface area and functional groups, particularly –NH sites, that facilitate adsorption and interaction with analyte molecules, thereby increasing selectivity. Thus, the interaction of rGO with PANI yields a synergistic composite with high conductivity, stability, and electroactive sites, exhibiting superior performance for electrochemical applications.

To the best of researchers' knowledge, the combination of rGO and PANI for the electrochemical detection of $NO_3^-$ has not been investigated in specific proportions. However, rGO/PANI nanocomposites have primarily demonstrated applicability to multiple analytes such as urea [20], ascorbic acid, dopamine and uric acid [21], lead and cadmium [22], nitrite [23], where they demonstrated enhanced sensitivity, selectivity, and stability because of the collective attributes of rGO, which has high surface area and excellent conductivity, and PANI, which has high redox activity and stability under environmental conditions. This lack of research emphasises the potential of rGO/PANI nanocomposites as a promising direction for future studies in $NO_3^-$ detection. Additionally, such a composite of rGO and CPs is already utilised in both enzymatic and non-enzymatic electrochemical determinations of $NO_3^-$. Although enzymatic $NO_3^-$ sensors are precise, they are often unstable, expensive, and sensitive to variations in storage conditions and potential interference. This makes them unsuitable for long-term or field environmental monitoring. On the contrary, non-enzymatic sensors do not have any biological components in their structure and rely solely on the electrocatalytic potential of the composite materials. They are usually more stable, less expensive, and suitable in challenging environments.

Thus, this study aims to synthesise rGO/PANI nanocomposite and explore its potential as a non-enzymatic electrochemical sensing platform for detecting $NO_3^-$ ions in environmental water samples. The rGO provides exceptional electrical conductivity and a high specific surface area, whereas PANI adds redox activity, ecological stability, and ease of polymerisation. However, each material faces challenges when used alone. By combining these two materials into a composite structure, this research aims to utilise their complementary physicochemical properties, thereby enhancing electrochemical activity, sensitivity, selectivity, and stability toward $NO_3^-$ detection. The originality of this research lies in the design and fabrication of rGO/PANI nanocomposite formulated explicitly for the electrochemical detection of $NO_3^-$ in environmental water samples.

## 2 Experimental

### 2.1 Materials

Graphite powder, sodium nitrate ($NaNO_3$), concentrated sulfuric acid ($H_2SO_4$), potassium permanganate ($KMnO_4$), hydrogen peroxide ($H_2O_2$), sodium carbonate ($Na_2CO_3$), aniline monomer, hydrochloric acid (HCl), ammonium persulfate (APS), dimethylformamide (DMF), potassium ferricyanide ($K_3[Fe(CN)_6]$), potassium chloride (KCl), sodium chloride (NaCl), sodium sulfate ($Na_2SO_4$), ethanol, sodium phosphate monobasic monohydrate ($NaH_2PO_4{\cdot}H_2O$), and sodium phosphate dibasic heptahydrate ($Na_2HPO_4{\cdot}7H_2O$) were purchased from Merck, Germany. NaCl, $Na_2SO_4$, potassium phosphate ($KHPO_4$), sodium bicarbonate ($NaHCO_3$), calcium chloride (CaCl), magnesium chloride ($MgCl_2$), and KCl were used for the study of interference measurements. The chemicals and solutions utilised were of analytical grade and were used as received, without further purification.

### 2.2 Synthesis of rGO

The rGO was synthesised from graphite through an intermediate compound known as graphene oxide (GO), which was typically prepared using the Hummers' method [24]. First, $KMnO_4$ was added slowly to the mixture to prevent

rapid reactions that could cause overheating. The oxidation process continued with constant stirring and slow warming, usually up to 35 to 40 °C, which allowed the graphite layers to separate and create GO. After a few hours, distilled water was carefully added, followed by $H_2O_2$ to stop the reaction. This resulted in a yellowish-green mixture, which indicated the formation of GO. The product was washed several times with deionised water, HCl, and ethanol using centrifugation to remove leftover salts and acids, and then it was dried to produce GO. To convert GO into rGO, a reduction process was required to eliminate the oxygen-containing functional groups and partially restore the conjugated carbon network. This reduction was achieved chemically using $Na_2CO_3$ as a reducing agent, as reported in a previous study [25]. The resulting product, known as rGO, retains many properties of pristine graphene, including a high surface area and good electrical conductivity, making it suitable for sensor applications.

### 2.3 Synthesis of PANI

To synthesise PANI for use in the nanocomposite, the aniline monomer was first protonated with HCl to facilitate oxidative polymerisation [26]. Different concentrations of HCl (0.5 M, 1 M, 1.5 M, and 2 M) were used to study the effect of acidity on the polymerisation process and the resulting properties of PANI. In each case, a fixed concentration of aniline was dissolved in the HCl solution under continuous stirring, and the mixture was maintained in an ice bath (0–5 °C) to control the reaction rate. The protonation of aniline forms anilinium ions, which are essential intermediates in the oxidative polymerisation process. Separately, an aqueous solution of APS, the oxidising agent, was prepared and added dropwise to the aniline-HCl mixture under vigorous stirring. The molar proportion of the APS to aniline ratio was kept at 1:1 so that the aniline could be oxidised fully. When APS was added, the solution eventually turned dark green instead of yellow, indicating that PANI had formed in the emeraldine salt form [27]. The reaction was allowed to proceed for several hours, after which the PANI was precipitated by filtration. It was then thoroughly washed with distilled water and ethanol to remove impurities and other unreacted reagents, and finally dried at room temperature.

### 2.4 Synthesis of rGO/PANI nanocomposite

The rGO/PANI nanocomposite was synthesised by adding as-prepared PANI during the chemical reduction of GO to rGO. Initially, GO was dispersed in an aqueous medium and sonicated to obtain a uniform suspension. Separately, PANI was synthesised via chemical oxidative polymerisation and then added to the GO dispersion. The GO with PANI solution was then mixed with a reducing agent, which facilitated the reduction of GO to rGO in the presence of PANI. This method enabled the PANI to blend well with the rGO sheets during reduction, resulting in a homogeneous rGO/PANI nanocomposite. The obtained material was dried by filtration under vacuum, washed, and then dried.

### 2.5 Material characterisations

All solutions were prepared using EASYpure LF deionised water from Barnstead. The ph levels of these water samples were measured with an Orion 720 A (MI, USA) pH meter. A Fourier Transform Infrared (FTIR) spectrum, employing the KBr disc method within a wavelength range of 400 $cm^{-1}$ to 4000 $cm^{-1}$, was obtained using the Agilent Cary 620/670 Series instrument. Surface nano-composite morphologies and microstructures were examined with a Hitachi SU-8020 UHR (Tokyo, Japan) field-emission scanning electron microscope (FESEM), revealing that PANI was uniformly dispersed on the rGO sheets. The presence of certain basic elements was confirmed by the electron dispersive X-ray (EDX) technique, used alongside FESEM. X-ray diffraction (XRD) measurements were conducted with a Bruker AXS (XRD: D8 Advance) using Cu Kα (1.54 Å) radiation as the source.

### 2.6 Electrode preparation and electrochemical measurements

The GCE interface was modified to a rGO/PANI composite film using the drop-casting technique. First, the rGO/PANI nanocomposite was dispersed in DMF to form an even suspension. After 30 min, it was sonicated to disaggregate and make it homogeneous. A carefully measured droplet of the well-dispersed rGO/PANI suspension was cast onto the polished sensor surface of the GCE using a micropipette. The droplet was dried to room temperature, where the solvent evaporated, leaving the composite material thinly coated across the electrode face. Cyclic voltammetry (CV) and square-wave voltammetry (SWV) were executed with a Potentiostat Gamry Series-G750 (Warminster, PA, USA). The electrodes used in this three-electrode system were Ag/AgCl, a platinum wire for the counter/auxiliary electrode, and rGO/PANI/GCE as the working electrode. CV measurements were performed in a 5 mM $K_3Fe(CN)_6$ solution in 0.1 M KCl. Electrochemical impedance spectroscopy (EIS) measurements were performed using a Gamry model Ref 3000 potentiostat/galvanostat (PA, USA), which produced a 10 mV amplitude sinusoidal AC signal from 0.01 Hz to 100 kHz. SWV was applied for the detection of $NO_3^-$ in the range of −0.25 V to 0.25 V with a 30 mV accumulation potential, a 40 Hz frequency, and a 40 mV pulse size. For all

other analyses and electrochemical measurements, nitrogen gas was purged through the electrolyte for 10 min to remove dissolved oxygen.

### 2.7 Real sample analysis

The real sample analysis involved collecting water samples from water bodies located in Tanjong Malim, Perak, Malaysia, which included lake and river systems. After collection and submission to the laboratory, the samples were first stored for no more than 48h under refrigeration at 4 °C and subsequently filtered through 0.45 µm membrane filters, which were designed to retain and remove suspended particles. For the electrochemical testing, the samples were brought to room temperature. Any sample which did not fall within the optimal pH range was brought within that range through the controlled addition of HCl or NaOH. To verify the sensor's reliability, recovery tests were conducted by spiking known amounts of $NO_3^-$ into the real water samples. In contrast, the analysed samples were subjected to the same electrochemical conditions as the standard solutions. Performance was evaluated using the average spectrum from three independent measurements of each sample [28]. Recovery was analysed through the value of the recovery factor, which is defined in Eq. 1:

$$\text{Recovery factor } (\%) = \frac{C_S - C_O}{C_A} \times 100 \quad (1)$$

Where $C_O$, $C_A$ and $C_S$ represent the concentration of the initial sample, the spiked concentration to the sample and the observed concentration of the spiked sample, respectively.

## 3 Results and discussion

### 3.1 Characterisation of rGO/PANI nanocomposites

The FTIR spectra of the samples in Fig. 1a illustrate the functional groups present in GO to rGO, and rGO/PANI nanocomposites synthesised with different HCl concentrations. The FTIR spectrum of GO exhibits a broad O–H peak at 3292 $cm^{-1}$, a sharp C=O peak at 1707 $cm^{-1}$, and a C=C peak at 1570 $cm^{-1}$, indicating the presence of hydroxyl,

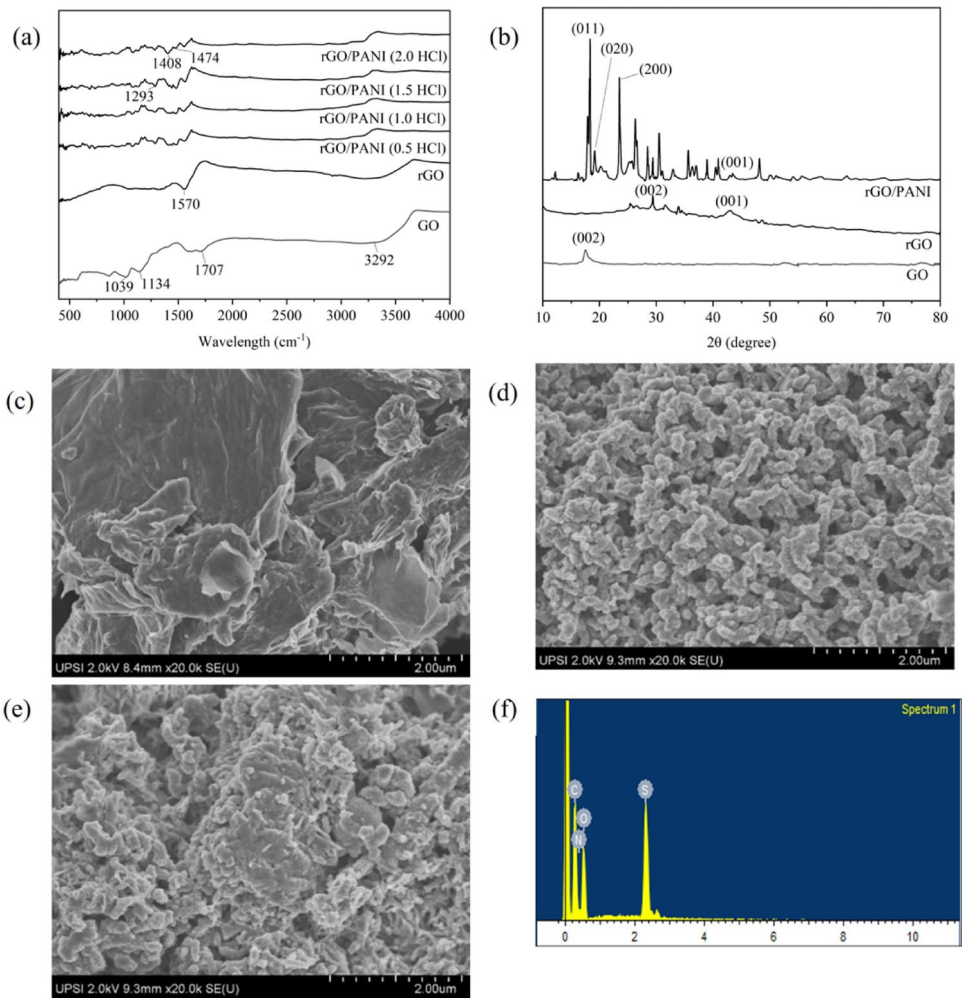


**Fig. 1** **a** The FTIR spectra of GO, rGO, and rGO/PANI composites synthesized at different HCl concentrations (0.5–2.0 M), **b** XRD patterns of samples, micrograph of **c** rGO, **d** PANI, **e** rGO/PANI nanocomposite, and **f** EDX analysis of rGO/PANI nanocomposite

carboxyl, and graphitic groups. Additional peaks at 1153, 1030, and 871 $cm^{-1}$ confirm the presence of oxygen-containing groups, such as C–O–C (epoxy), C–O (alkoxy), and out-of-plane C–H bending vibrations [29]. The FTIR spectrum of rGO shows apparent differences compared to GO, indicating that the reduction was successful. In rGO, these oxygen-related peaks are weaker or reduced, especially the O–H and C=O bands, showing successful reduction. In the rGO/PANI nanocomposites, new peaks emerged at 1293 $cm^{-1}$, 1408 $cm^{-1}$, and 1478 $cm^{-1}$, attributed to C–N stretching vibrations of benzenoid rings, along with C=N bands related to the quinoid and benzenoid C–H stretching of PANI [30]. These characteristic PANI peaks became increasingly intense and well-defined as the HCl concentration increased, particularly at concentrations of 1.5 and 2.0 M. However, at 2.0 M HCl, the PANI peaks are still there but indicate some broadening and shifting. This change could result in overdoping, which may lead to structural distortion [31]. Overall, the composite prepared with 1.5 M HCl exhibits the most well-defined functional groups and optimal doping characteristics, making it the most favourable formulation.

Figure 1b presents the XRD patterns of GO, rGO, and the rGO/PANI nanocomposite, clearly showing the structural changes resulting from the chemical reduction of GO and subsequent compositing with PANI. The GO sample displays a characteristic diffraction peak at $2\theta \approx 12°$ corresponding to the (001) plane, indicative of its highly oxidised structure. After reduction, this peak disappears and is replaced by a broad peak at $2\theta \approx 26°$ (002 plane) in rGO, indicating the partial restoration of the $sp^2$ carbon network and a decrease in interlayer spacing. In contrast, the rGO/PANI nanocomposite exhibits multiple sharp, well-defined peaks between $2\theta = 15–30°$ corresponding to the (011), (020) and (200) planes, confirming the presence of semi-crystalline PANI in its conductive emeraldine salt form. These peaks demonstrate that incorporation of PANI imparts a higher degree of structural order to the composite. The overall XRD pattern confirms successful formation of the rGO/PANI nanocomposite, with features from both rGO and PANI clearly visible. The enhanced crystallinity of the composite is attributed to strong interactions between the rGO sheets and PANI chains, which promote a more ordered structural arrangement than rGO alone.

The FESEM micrographs clearly illustrate the morphological differences between Fig. 1 (c) rGO, (d) PANI, and (e) the rGO–PANI nanocomposite. The rGO exhibits a wrinkled, crumpled, and layered sheet-like structure with voids and folds that prevent restacking and provide a large surface area for electrochemical activity. In contrast, PANI exhibits a nanostructured, granular, and agglomerated morphology with cauliflower-like clusters, typical of PANI synthesised via oxidative polymerisation. This morphology yields a porous network with abundant electroactive sites, but exhibits limited conductivity compared to rGO-based materials. When rGO and PANI are combined, the resulting rGO–PANI nanocomposite demonstrates a synergistic morphology in which rGO sheets act as a conductive backbone uniformly decorated with nanostructured conducting PANI particles. The composite effectively integrates the high conductivity and surface area of rGO with the redox activity of PANI, making it highly suitable for electrochemical sensing.

The elemental composition of the rGO/PANI composite was investigated by EDX in Fig. 1f. The spectrum revealed the presence of carbon (C), oxygen (O), nitrogen (N), and sulfur (S). Carbon was the dominant element (47.77 wt%, 57.11 at%), originating mainly from the rGO backbone and the carbon-rich PANI structure. Oxygen (27.94 wt%, 25.08 at%) was attributed to residual oxygen-containing functional groups in rGO, as well as possible contributions from PANI. The PANI component, a conducting polymer rich in nitrogen-containing groups such as amines and imines, contributes nitrogen (12.01 wt%, 12.31 at%). The presence of sulfur (12.27 wt%, 5.50 at%) likely comes from the doping or polymerisation process of PANI. The presence of these elements confirms the successful doping of PANI and the intense interaction with the rGO matrix. The EDX results confirm the successful synthesis of the rGO/PANI nanocomposite, with clear evidence of the elemental components characteristic of both rGO and PANI.

### 3.2 Electrochemical characteristics

The electrochemical behaviour of PANI/GCE, rGO/PANI, and rGO/PANI/GCE was examined using CV in the range from −0.25 to 0.3 V versus Ag/AgCl reference electrode, recorded at a 100 mV $s^{-1}$ scan rate in the 5 mM solution of $K_3Fe(CN)_6$ in 0.1 M KCl. The observed shapes of the peaks depicted in Fig. 2a indicate that the rGO/PANI/GCE delivers a markedly higher current response than either rGO/GCE or PANI/GCE, with cathodic currents of 29 µA compared with 14 µA and 6 µA, respectively, and an end-of-scan current reaching. The PANI/GCE exhibits electrical conductivity and weakly defined redox features, indicating the propagation of a faradaic reaction. This is attributed to the redox transitions of PANI between the leucoemeraldine, emeraldine, and pernigraniline states, with the emeraldine salt form providing PANI's conductivity due to its delocalised charge carriers [32]. However, the low intensity of the redox peaks indicates the need for improvements in charge-storage kinetics within the material. Meanwhile, the electrical conductivity of rGO/GCE is attributed to the reduction of GO, which restores its conjugated π–π network, thereby enhancing conductivity and increasing the

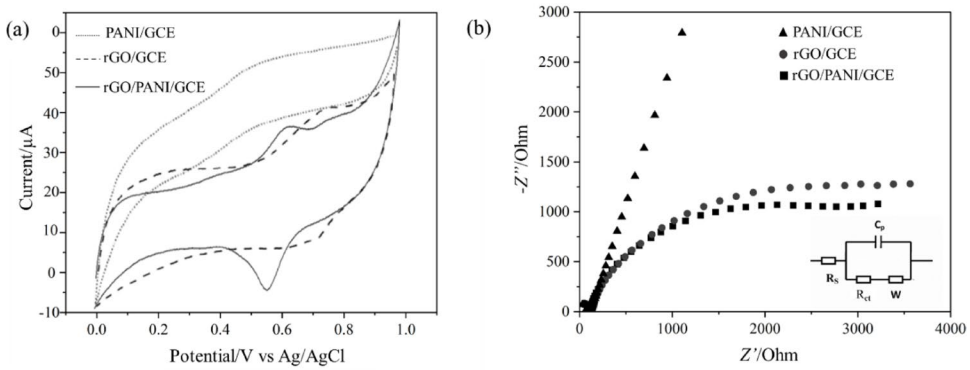


**Fig. 2** **a** CV and **b** EIS analysis of the fabricated electrodes

electroactive surface area, consistent with the findings of Li et al. [33]. The CV profiles for these electrodes are broad and quasi-rectangular, rather than exhibiting sharp, well-defined peaks, indicating fast, reversible surface redox reactions typical of pseudocapacitive behaviour. This behaviour arises from the combined contributions of PANI, which provides multiple redox-active sites for faradaic charge storage, and rGO, which offers a highly conductive framework with a large surface area, enabling fast electron transport and double-layer formation. These effects improve charge-transfer kinetics and increase the accessible active area. As a result, rGO/PANI/GCE exhibits a greater capacitive-type response and better electrochemical performance.

The Nyquist plot analysis further supports the electron transfer characteristics of the fabricated sensors (Fig. 2b). The inset shows the equivalent circuit used to model the EIS data, which is a modified Randles circuit. It includes the solution resistance ($R_s$), the charge-transfer resistance ($R_{ct}$), a constant-phase element ($C_p$) representing the non-ideal double-layer capacitance, and a Warburg element (W) [34]. The PANI/GCE exhibits the highest values of both real ($Z'$) and imaginary ($-Z''$) impedance, with a high $R_{ct}$ value (800 Ω) and low conductivity. This behaviour shows that PANI alone typically exhibits limited electrical conductivity in the absence of conductive supports. The rGO/GCE exhibits better conductivity ($R_{ct}$ = 500 Ω) than the PANI/GCE, but it is still not the most efficient. The lowest impedance values ($R_{ct}$ = 300 Ω) signified the best electron transfer kinetics among the three electrodes. The combination of the lowest $R_{ct}$, the highest peak currents in CV, and the largest electrochemical surface area (ECSA) confirms that the rGO/PANI/GCE offers the most efficient electrochemical interface, making it highly favourable for electrochemical sensing detection.

### 3.3 Electrochemical surface area

The ECSA studies of PANI/GCE, GO/GCE and PANI/GO/GCE sensor was calculated using the Randles–Sevcik equation (Eq. 2):

$$I = \left(2.69 \times 10^{-5}\right) \mathrm{ACD}^{1/2}\, \mathrm{n}^{3/2}\, v^{1/2} \quad (2)$$

Where A represents the effective surface area of the electrodes in $cm^2$, n is the number of electrons taking part in the charge transfer process, D is the diffusion coefficient of the analyte in the solution, and C is the concentration of $K_3Fe(CN)_6$ solution. The values of n and D for $K_3Fe(CN)_6$ are 1 and $7.6 \times 10^{-6}$ $cm^2$ $s^{-1}$, respectively. The obtained results reveal that the PANI/GO/GCE nanocomposite sensor possesses a greater surface area (0.2134 $cm^2$) than PANI/GCE (0.1558 $cm^2$), and GO/GCE (0.1033 $cm^2$), suggesting an enhanced electrocatalytic performance of the fabricated PANI/GO/GCE. The synergistic interaction between rGO and PANI, where rGO provides a highly conductive scaffold for efficient electron transport while PANI contributes abundant redox-active sites, enhances the electrochemical surface area of the fabricated sensor.

### 3.4 Optimisation of the experimental parameters for $NO_3^-$ detection

In the CV analysis using $Na_2SO_3$ as the supporting electrolyte, apparent variations in the electrochemical responses of the electrodes towards $NO_3^-$ detection were observed (Fig. 3a). The bare GCE showed no detectable current response, indicating poor catalytic activity. With PANI modification, the current response improved to 9 µA due to enhanced conductivity and the presence of electroactive nitrogen groups. The incorporation of GO/GCE further increased the response (14 µA), facilitated by oxygen-containing functionalities that aid the charge transfer. A more significant enhancement was observed for rGO/GCE, which delivered a peak current of 20 µA, reflecting the superior electron mobility and large surface area of graphene nanosheets. Most importantly, the rGO/PANI/GCE electrode exhibited the highest electrochemical activity, with a current response of 27 µA. This remarkable increase highlights the strong synergistic interaction between rGO and PANI, which not

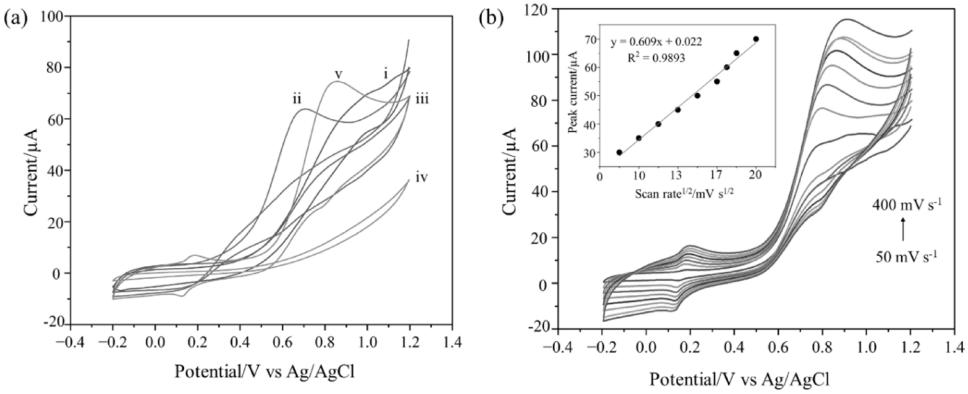


**Fig. 3** **a** Voltammograms of (i) GO/GCE, (ii) rGO/GCE, (iii) PANI/GCE, (iv) bare GCE, and (v) rGO/PANI–GCE towards $NO_3^-$ detection in 0.02 M $Na_2SO_4$ electrolyte with a scan rate of 100 mV $s^{-1}$, and **b** voltammograms of the rGO/PANI/GCE in 0.02 M $Na_2SO_4$ electrolyte at different scan rates from 50 to 400 mV $s^{-1}$ (inset shows the plot of peak current versus the square root of scan rate)

.

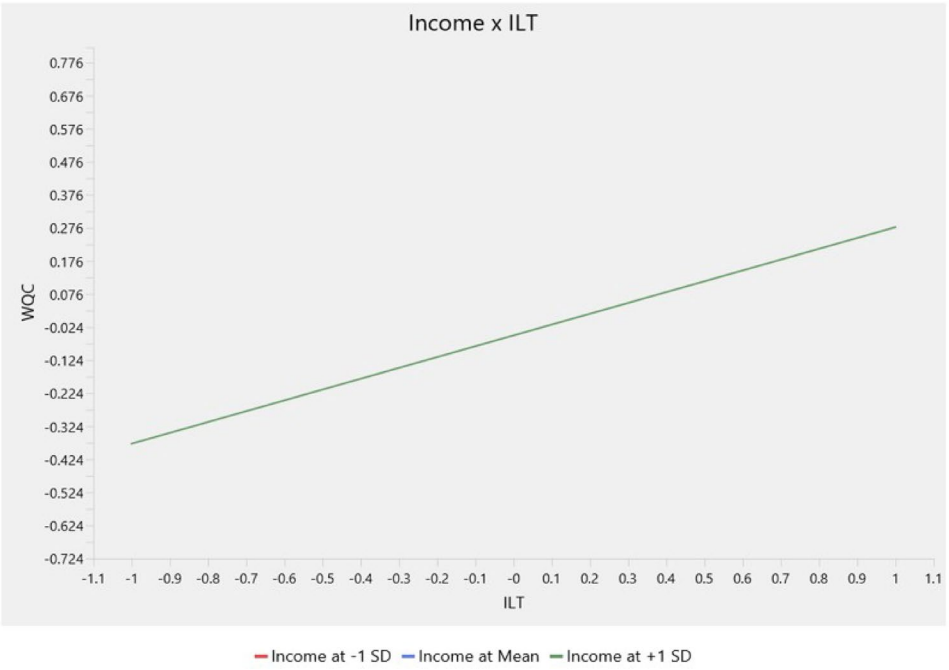


only reduced the overpotential for $NO_3^-$ reduction but also enhanced charge transfer kinetics.

The CV of the rGO/PANI/GCE clearly changes with scan rate, ranging from 50 to 400 mV $s^{-1}$ (Fig. 3b). As the scan rate increases, the redox peak currents rise. This indicates improved charge-transfer kinetics and a surface- or mixed-controlled electrochemical process. The peaks become slightly broader and shift as the scan rate increases, suggesting quasi-reversible behaviour [35]. The inset plot of peak current versus the square root of scan rate yields a linear relationship ($I_p$ = 0.609 v+0.022, $R^2$ = 0.9893), The inset plot of peak current versus the square root of the scan rate shows a linear relationship ($I_p$ = 0.609v+0.022, $R^2$ = 0.9893), indicating that the redox response is mainly surface-controlled by adsorption or pseudocapacitive [36]. This behaviour benefits $NO_3^-$ detection by enabling rapid electron transfer and producing higher current responses at increasing scan rates.

### 3.5 Effect of pH

Figure 4a shows the SWV responses recorded at different pH levels, ranging from 6.6 to 7.2. At pH 7.0, the peak current (37.51 µA) is highest and a sharp, well-defined peak is observed around 0.12 V, suggesting this pH offers the most suitable environment for the redox process, likely due to an optimal balance of proton availability and electron transfer kinetics. As the pH deviates from 7.0 in either direction, the peak current decreases, indicating reduced electrochemical activity. Conversely, both slightly acidic (pH 6.6) and slightly alkaline (pH 7.2) conditions produce lower peak currents. The detection mechanism of $NO_3^-$ via electrochemical methods primarily involves the electrocatalytic reduction at the surface of the modified working electrode, which requires the simultaneous transfer of protons and electrons (Eq. 3).

$$NO_3^- + 2H^+ + 2e^- \rightarrow NO^2 + H_2O \quad (3)$$

Scheme 1 illustrates the proton-coupled electron transfer (PCET) mechanism for the electrochemical reduction of $NO_3^-$ on a modified rGO/PANI/GCE surface. In the electrolyte, $NO_3^-$ and protons ($H^+$) from the acidic medium diffuse toward the electrode, where active sites such as doped polyaniline or catalytic nanoparticles adsorb the $NO_3^-$ species. Electrons supplied from the external circuit travel through the conductive electrode and are simultaneously injected into the adsorbed $NO_3^-$ ions, along with protons arriving from the solution. Through two successive proton–electron additions, the adsorbed $NO_3^-$ is reduced to nitrite ($NO_2^-$) and water, which then desorb back into the electrolyte. This coupling of electron delivery from the electrode and proton supply from the electrolyte lowers the reaction's activation energy, enabling efficient $NO_3^-$ reduction and providing the basis for the current response in electrochemical $NO_3^-$ sensors [37, 38].

At a very acidic pH, the medium contains a high concentration of hydrogen ions, also known as protons. However, the $NO_3^-$ gets increasingly pushed away by the positively charged, highly protonated PANI surface. It can also undergo competing side reactions, which reduce the apparent catalytic current. At a very alkaline pH, the surface is favourable for $NO_3^-$ attachment, but proton availability becomes limited, slowing the PCET steps. As a result, the current decreases again, and the peak moves to more negative potentials. At a neutral pH (approximately 7), an ideal balance exists: there are sufficient protons for rapid PCET, and the PANI film is partially protonated. This allows it to work as a proton shuttle without repelling $NO_3^-$ too strongly, keeping it more stable and highly soluble [39]. This combination maximises adsorption, electron transfer, and proton supply simultaneously, resulting in the highest observed peak current at pH 7.

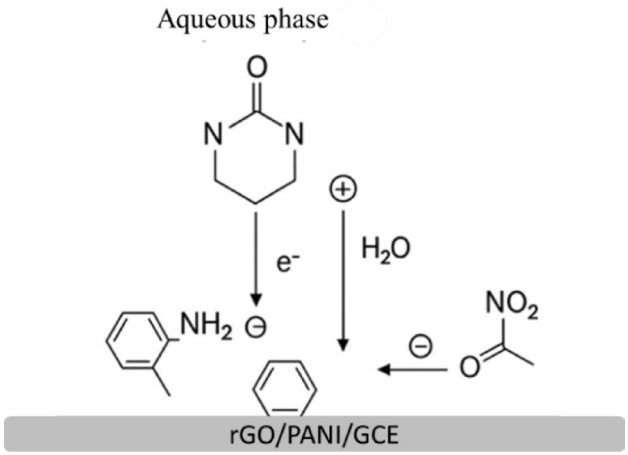


**Scheme 1** Illustration of the mechanism of electrocatalytic $NO_3^-$ detection at the surface of rGO/PANI/GCE

### 3.6 Type of electrolyte

Figure 4b shows the electrochemical behaviour of the rGO/PANI/GCE electrode for $NO_3^-$ detection in different electrolytes. Among the tested media, $Na_2SO_4$ produces the highest peak current, indicating faster electron transfer and more favourable reduction kinetics for $NO_3^-$ compared with the other electrolytes. This enhanced response is attributed to the high ionic conductivity of $Na_2SO_4$ and its relatively low level of interfering species, which together promote the dominant redox reactions at the electrode surface. In contrast, NaCl and PBS yield only moderate peak currents, suggesting poorer ionic conduction or competition from other ionic species such as $Cl^-$ and $PO_4^{3-}$. NaCl in particular gives the lowest current response, likely due to interference from potassium and chloride ions, which may form ionic structures with $NO_3^-$ that reduce its mobility and hinder its access to the electrode surface [40]. The overall trend across the data confirms that $Na_2SO_4$ outperforms the other electrolytes, highlighting the importance of selecting an appropriate electrolyte to maximise the sensor's sensitivity and efficiency.

### 3.7 Concentration of electrolyte

The effect of electrolyte concentration on the detection of $NO_3^-$ ions was also systematically investigated (Fig. 4c). The reaction current of the solution containing 0.005 M $Na_2SO_3$ was significantly lower, attributed to the low ionic strength and limited ion mobility, which hindered electron crossover at the working electrode surface. There was a significant increase in current at the 0.02 M concentration level, attributed to increased ionic conductivity and favourable rates of diffusion of $NO_3^-$ ions and the electron-transfer reaction. Beyond this concentration level, however, further increments to 0.04 M and 0.06 M were accompanied by a gradual decline in current response. Such a decline has been explained by increased solution viscosity, ion pairing, and anion shielding, which reduce the supply of $NO_3^-$ to the electrode surface [41]. The inset graph also shows the current increase, which confirms that this is the optimal electrolyte concentration for best sensitivity and performance of the sensor.

### 3.8 Optimisation of the parameters of SWV

The study has shown that well-considered and optimised SWV parameter values, such as potential accumulation, frequency, and pulse size, should ensure optimal signal

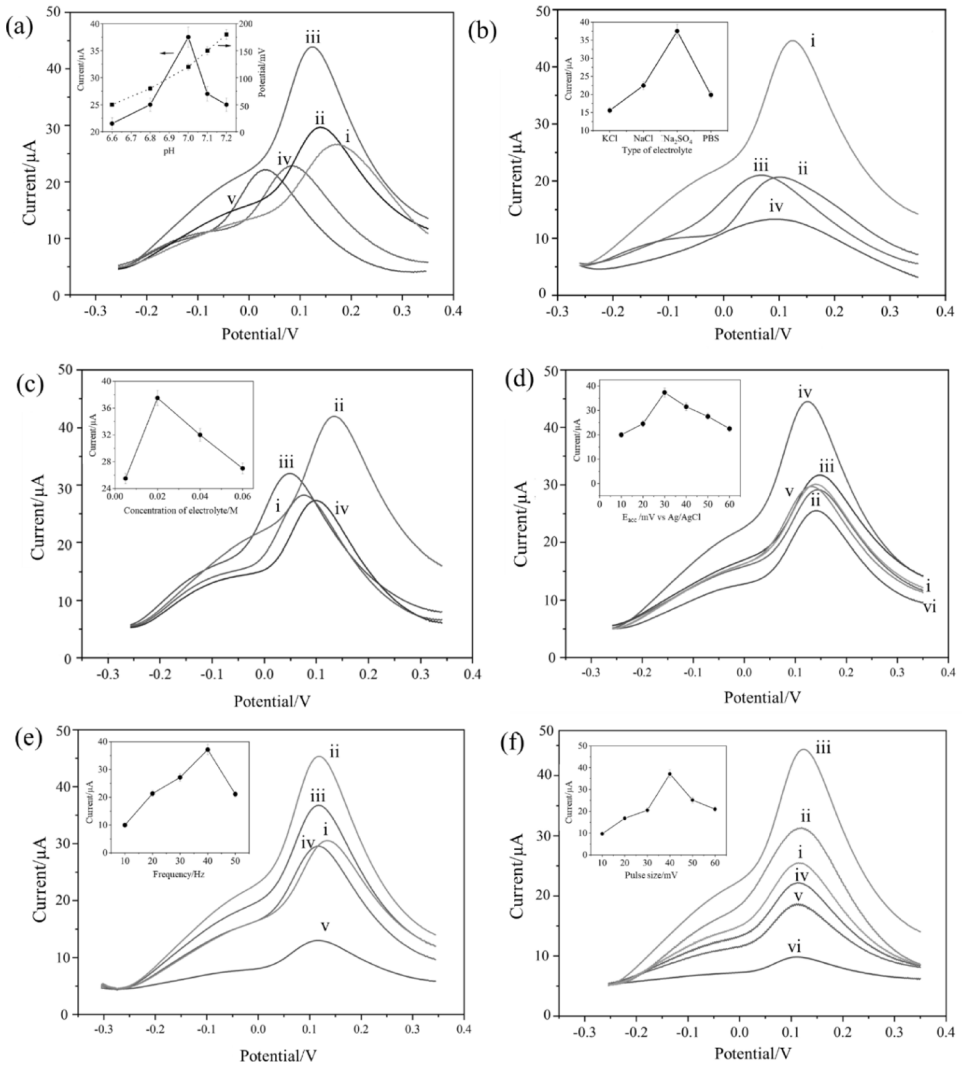


**Fig. 4** Optimisation of the experimental parameters with **a** pH values: (i) 7.2, (ii) 7.1, (iii) 7.0, (iv) 6.8, and (v) 6.6, **b** effect of electrolyte type on $NO_3^-$ detection performance: (i) $Na_2SO_4$, (ii) PBS, (iii) NaCl, and (iv) KCl, **c** effect of electrolyte concentration on $NO_3^-$ detection: (i) 0.005 M, (ii) 0.02 M, (iii) 0.04 M, and (iv) 0.06 M, and the SWV parameters of **d** accumulation potential, $E_{acc}$/mV vs. Ag/AgCl: (i) 60, (ii) 50, (iii) 40, (iv) 30, (v) 20, and (vi) 10, **e** frequency, Hz: (i) 50, (ii) 40, (iii) 30, (iv) 20, and (v) 10, and **f** pulse size: (i) 60, (ii) 50, (iii) 40, (iv) 30, (v) 20, and (vi) 10

strength, thereby affirming the functionality of the SWV method as an apparatus for the electrochemical detection of $NO_3^-$ using rGO/PANI/GCE. Accumulation represents a parameter that determines the retention of analyte ions and their concentration at the electrode surface. The potential must be kept within a threshold, as it is either too small or too large; values outside this range would lead to improper functioning, resulting in the adsorption or removal of the surface form of the reactants [42]. As shown in Fig. 4d, the highest sustainable current at any given point within the sensor occurs at an accumulation potential of 40 mV. This current at a potential of 40 mV reflects saturation, during which the highest amount of $NO_3^-$ can be absorbed and simultaneously desorbed. Below the potential of 40 mV, at 10 and 30 mV, the current rises linearly, which, in this case, may be interpreted as the potential response to the concentration of $NO_3^-$ at the electrode surface. However, at potentials above 40 mV, such as 50 and 60 mV, the current magnitude diminishes. This decline may, in part, be attributed to surface saturation, where multiple ions can be adsorbed, leading to the displacement of $NO_3^-$ [43].

Both the speed of electron-transfer processes and background capacitive currents impose limits on the lower and upper ends of the current frequency spectrum. Any increase in frequency will likely increase signal strength and possibly influence the focal geometry of the peaks, due to the relatively slow electron-transfer kinetics. In contrast, lower frequencies exhibit higher-resolution signal differentiation but lower signal sensitivity [42]. Figure 4e shows the effect of frequency on the electrochemical signal responsiveness of the rGO/PANI/GCE and its electrochemical current response. At these frequencies, the current appears to be revised to the lower limit of the sensor's design. 10 and 20 Hz operate at such lower frequencies. At these frequencies, potential can change more slowly, indicating that electron transfer, as well as the rate of $NO_3^-$ reduction, must be slow to avoid reaching a bottleneck. For the majority of other frequencies assessed, 30 Hz and, in particular, the range of

40 to 60 Hz, the peak current was depressed. At rest, a 30 Hz frequency achieves the highest current, while frequencies between 40 and 60 Hz also achieve the highest current. Stimulation of these is likely to be caused by inadequate time supplied with other control potentials in the cycle for complete scavenging of electron reactions from the skipped signal. This supports the notion that the frequency of the SWV on the sensor counter electrode directly affects the net sensor sensitivity.

The amplitude of a pulse, or its size, determines the extent of the current response. Pulse amplitude enhancement increases the faradaic signal while simultaneously aggravating background noise and broadening peaks. In comparison, smaller pulses offer greater sensitivity but at the cost of resolution [42]. Pulse size in the electrochemical response of the rGO/PANI/GCE is shown in Fig. 4f. The peak current increases with increasing pulse amplitude from 10 mV to 60 mV. This suggests that the sensor sensitivity is directly proportional to pulse amplitude. The increased current response suggests an elevated rate of electron transfer, and the signal output pulse size is directly proportional to this increase, indicating enhanced electron transfer. Notably, although the amplitudes differ, the maximum potential appears relatively constant. This suggests that the redox reaction mechanism is probably the same. Hence, the optimum response is recorded at a pulse size of 40 mV.

### 3.9 Performance for $NO_3^-$ determination

As shown in Fig. 5a, the calibration curve was generated by plotting peak current response (μA) against analyte concentration (μM). The sensor exhibited a strong linear response across the range of 7–45 μM, described by the regression equation $I = 22.943 + 0.863$ C, where $I$ is the peak current (μA), and C is the analyte concentration (μM). The high correlation coefficient ($R^2 = 0.982$) confirms excellent linearity and dependable analytical performance within this range. The sensor achieved a low detection limit of 1.74 μM and a sensitivity of 0.863 μA $\mu M^{-1}$, emphasising its high sensitivity and suitability for detecting $NO_3^-$. Various sensor types have been developed for analyte detection, utilising both enzymatic and non-enzymatic methods (Table 1). Overall, the comparison highlights the advantages and disadvantages of enzymatic and non-enzymatic sensors, with non-enzymatic sensors showing higher limits of detection but lower stability. Conversely, enzymatic sensors have lower limits of detection but offer a greater linear range.

### 3.10 Selectivity, reproducibility, and stability

The electrode's selectivity was determined with typical ions and potential interference found in natural and drinking waters (Fig. 5b). Possible interferents with chloride ($Cl^-$), sulfate ($SO_4^{2-}$), phosphate ($PO_4^{3-}$), nitrite ($NO_2^-$), bicarbonate ($HCO_3^-$), calcium ($Ca^{2+}$), magnesium ($Mg^{2+}$),

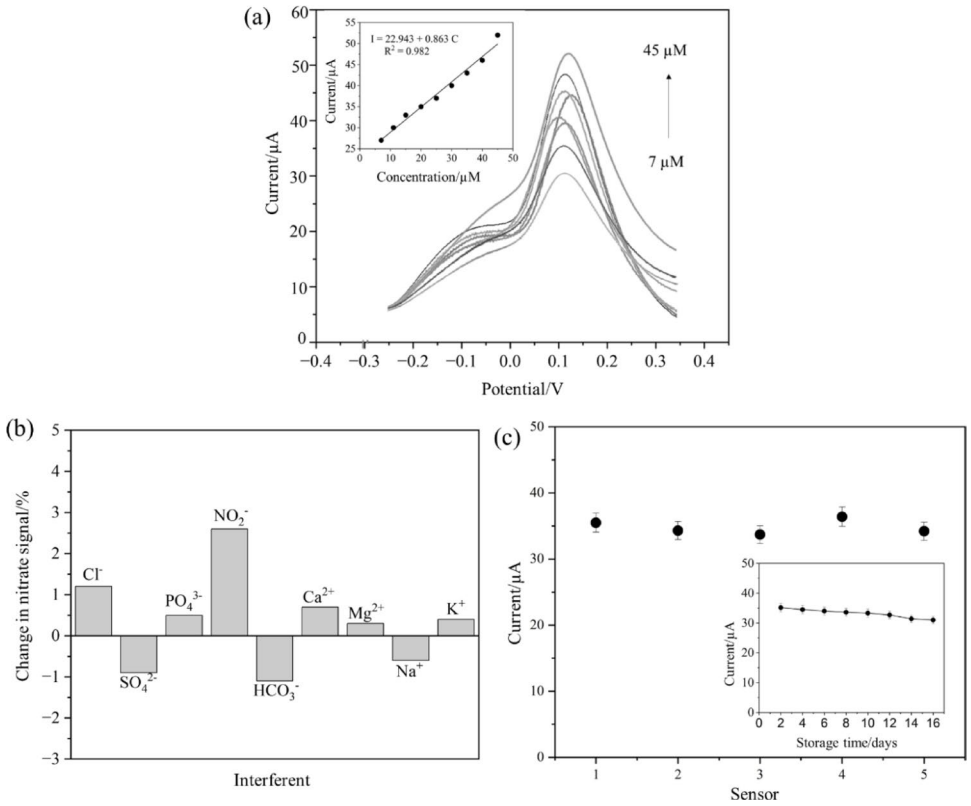


**Fig. 5** **a** SWV responses of rGO/PANI/GCE with successive addition of $NO_3^-$ (inset shows the plot of current response vs. concentration of $NO_3^-$ at rGO/PANI/GCE, **b** interferences study, and **c** reproducibility (inset shows the stability of the sensor)

**Table 1** In comparison with previous studies that employed rGO and/or conducting polymer nanocomposites for $NO_3^-$ detection

| Sensor | Technique | Enzymatic/Non-enzymatic | Linear range (µM) | LOD (µM) | Sensitivity (µA $µM^{-1}$) | References |
|---|---|---|---|---|---|---|
| GCE/RGO/Ppy/NR | CV | Enzymatic | 5,000 to 20,000 | 275 | – | [44] |
| PPy–NaR–NADH | Amperometric | Enzymatic | 10 to 500 | 0.20 | – | [45] |
| GA@PANI-CNT | SWV | Non-enzymatic | 1–10<br>15–50 | 0.42 | – | [46] |
| rGO aerogel | Potentiometric | Non-enzymatic | 1 to 100 | 0.759 | – | [47] |
| PEDOT nanowire | Amperometric | Enzymatic | Not specified | 0.888 | 92.00 | [48] |
| IIP-Cu-NPs/PANI | EIS and LSV[a] | Non-enzymatic | 1–10,000 | 31 and 5 | – | [49] |
| rGO/PANI/GCE | SWV | Non-enzymatic | 7 to 45 | 1.74 | 0.863 | This work |

[a]linear sweep voltammetry

sodium ($Na^+$), and potassium ($K^+$) were defined for 20 µM of $NO_3^-$. Each interfering species was diluted 10- to 100-fold with $NO_3^-$ to mimic natural scenarios. Most ions caused insignificant changes in current response (±5%) for $NO_3^-$. In particular, $Cl^-$ and $SO_4^{2-}$, at the highest concentrations, were still not significant to the peak current with $NO_3^-$ and thus may be considered interfering ions. Despite the similarity in redox potential, $NO_2^-$ produced a minor overlapping signal that remained below 10% under the defined conditions. Thus, the sensor demonstrates high selectivity for $NO_3^-$ with the presence of many interferences or potential confounding species.

The reproducibility of the GO/PANI/GCE sensor was determined using five single, prepared sensors (Fig. 5c). As shown in the plot, the current values of all sensors fall within a tight band of approximately 34 to 37 µA. The variation among the sensors was also minimal, with the highest deviation of approximately 3 µA, or about a 10% difference. Quantitative data have revealed a mean current of 34.7 µA and a relative standard deviation of 2.99%, further confirming the method's accuracy. These results indicate that the rGO/PANI/GCE sensor fabrication process is sustainable and consistent, yielding extremely reproducible electrochemical characteristics in devices. The current response of the sensor is presented in the SWV graph over 16 days. A slight change in the current values, with a distinction of no more than 4 µA between the second and 16th day, demonstrates the sensor's stability when used over a long period.

### 3.11 Real sample analysis

Different real environmental water samples (river and lake water) were used to conduct tests to recover the rGO/PANI/GCE sensor constructed within the study. Using the sensor, samples with known spikes of the analyte (10, 20, and 30 µM) were measured (Table 2). The recovery values of the samples were all within 95–105%, which is more than enough to validate the accuracy of the method. The technique also demonstrated good accuracy, as indicated by the relative standard deviation (RSD) values, which were consistently below 3% for all measurements. These findings

**Table 2** Recovery test results for analyte detection in real water samples

| Sample | Added concentration (µM) | Measured concentration (µM) | Recovery (%) | RSD |
|---|---|---|---|---|
| River water | 10 | 9.8 ± 0.2 | 98.0 | 2.04 |
| | 20 | 19.1 ± 0.4 | 95.5 | 2.09 |
| | 30 | 31.2 ± 0.9 | 104.0 | 2.88 |
| Lake water | 10 | 10.2 ± 0.3 | 102.0 | 2.55 |
| | 20 | 19.5 ± 0.5 | 98.0 | 2.88 |
| | 30 | 28.7 ± 0.4 | 95.7 | 1.39 |

are consistent with previous studies [50, 51]. In conclusion, these findings confirm that the analytical method used is reliable and valid for quantifying $NO_3^-$ in environmental water samples.

## 4 Conclusion

This work introduces a non-enzymatic reduced graphene oxide/polyaniline (rGO/PANI) nanocomposite electrode for the electrochemical detection of $NO_3^-$ in environmental water, achieving good sensitivity, low detection limits, and excellent selectivity. The integration of PANI into the rGO structure was confirmed through detailed structural and morphological characterisations, resulting in a conductive nanocomposite. Electrochemical studies (CV, EIS, and SWV) demonstrated excellent electrocatalytic activity toward $NO_3^-$ detection. Further optimisation of type and supporting electrolytes, pH, and SWV parameters enhanced electron-transfer kinetics. The sensor exhibited remarkable reproducibility, stability, and applicability to real environmental water samples, highlighting the potential of rGO/PANI nanocomposites as a cost-effective, stable, and versatile platform for the ecological monitoring of $NO_3^-$ contaminants in water, thereby advancing microanalytical techniques for the detection of trace contaminants.

**Acknowledgements** Financial support from the Kurita Water and Environment Foundation (Grant No. 2021-0239-103-11) is gratefully acknowledged. The authors also thank Universiti Pendidikan Sultan Idris for providing support and facilities that enabled the successful

completion of this work.

**Author contributions** Siti Nur Akmar Mohd Yazid: Methodology, Validation, Investigation, Writing—original draft.Mohamad Idris Saidin: Methodology, Visualisation, Data curation.Illyas Md Isa: Data curation, Visualisation, Validation.Chin Suk Fun: Data curation, Visualisation.Ain Nadirah Romainor: Investigation, Visualisation, Writing—Review & Editing.Nur Indah Wardani: Investigation, Visualisation, Writing—Review & Editing.Mohamad Syahrizal Ahmad: Methodology, Investigation.All authors have read and approved the final manuscript.

**Funding** Open access funding provided by The Ministry of Higher Education Malaysia and Universiti Pendidikan Sultan Idris. This work was supported by Kurita Water and Environment Foundation under Grant No. 2021-0239-103-11.

**Data availability** No datasets were generated or analysed during the current study.

## Declarations

**Conflict of interest** The authors declare that they have no known competing financial interests or personal relationships that could have appeared to influence the work reported in this paper.

**Clinical trial number** Not applicable.



## References

1. Singh B, Craswell E (2021) Fertilizers and nitrate pollution of surface and ground water: an increasingly pervasive global problem. SN Appl Sci 3:518. https://doi.org/10.1007/s42452-021-04521-8
2. Smith VH, Tilman GD, Nekola JC (1999) Eutrophication: impacts of excess nutrient inputs on freshwater, marine, and terrestrial ecosystems. Environ Pollut 100:179–196. https://doi.org/10.1016/S0269-7491(99)00091-3
3. Camargo JA, Alonso Á (2006) Ecological and toxicological effects of inorganic nitrogen pollution in aquatic ecosystems: a global assessment. Environ Int 32:831–849. https://doi.org/10.1016/j.envint.2006.05.002
4. Wang L, Lin K, Guo H, Zhang Y (2022) Spectrophotometric determination of nitrate in small volume of seawater samples using a simple resorcinol method. Anal Bioanal Chem 414:5869–5876. https://doi.org/10.1007/s00216-022-04152-x
5. Coviello D, Pascale R, Ciriello R, Salvi AM, Guerrieri A, Contursi M, Bianco G (2020) Validation of an analytical method for nitrite and nitrate determination in meat foods for infants by ion chromatography with conductivity detection. Foods 9:1238. https://doi.org/10.3390/foods9091238
6. Murray E, Nesterenko EP, McCaul M, Morrin A, Diamond D, Moore B (2017) A colorimetric method for use within portable test kits for nitrate determination in various water matrices. Anal Methods 9:680–687. https://doi.org/10.1039/C6AY03190K
7. Lal K, Jaywant SA, Arif KM (2023) Electrochemical and optical sensors for real-time detection of nitrate in water. Sensors 23:7099. https://doi.org/10.3390/s23167099
8. Tan JF, Anastasi A, Chandra S (2022) Electrochemical detection of nitrate, nitrite and ammonium for on-site water quality monitoring. Curr Opin Electrochem 32:100926. https://doi.org/10.1016/j.coelec.2021.100926
9. Ryu H, Thompson D, Huang Y, Li B, Lei Y (2020) Electrochemical sensors for nitrogen species: a review. Sensors and Actuators Reports 2:100022. https://doi.org/10.1016/j.snr.2020.100022
10. Jiang C, He Y, Liu Y (2020) Recent advances in sensors for electrochemical analysis of nitrate in food and environmental matrices. Analyst 145:5400–5413. https://doi.org/10.1039/D0AN00823K
11. Justino CI, Gomes AR, Freitas AC, Duarte AC, Rocha-Santos TA (2017) Graphene based sensors and biosensors. TrAC Trends Anal Chem 91:53–66. https://doi.org/10.1016/j.trac.2017.04.003
12. Nag A, Mitra A, Mukhopadhyay SC (2018) Graphene and its sensor-based applications: a review. Sens Actuators A Phys 270:177–194. https://doi.org/10.1016/j.sna.2017.12.028
13. Ambrosi A, Chua CK, Bonanni A, Pumera M (2014) Electrochemistry of graphene and related materials. Chem Rev 114:7150–7188. https://doi.org/10.1021/cr500023c
14. Reddy YVM, Shin JH, Palakollu VN, Sravani B, Choi CH, Park K, Shetti NP (2022) Strategies, advances, and challenges associated with the use of graphene-based nanocomposites for electrochemical biosensors. Adv Colloid Interface Sci 304:102664. https://doi.org/10.1016/j.cis.2022.102664
15. Hasan MB, Parvez MM, Abir AY, Ahmad MF (2025) A review on conducting organic polymers: concepts, applications, and potential environmental benefits. Heliyon. https://doi.org/10.3390/polym13122003
16. Das TK, Prusty S (2012) Review on conducting polymers and their applications. Polym-Plast Technol Eng 51(14):1487–1500. https://doi.org/10.1080/03602559.2012.710697
17. Beygisangchin M, Abdul Rashid S, Shafie S, Sadrolhosseini AR, Lim HN (2021) Preparations, properties, and applications of polyaniline and polyaniline thin films—a review. Polymers 13:2003. https://doi.org/10.3390/polym13122003
18. Gospodinova N, Terlemezyan L (1998) Conducting polymers prepared by oxidative polymerization: polyaniline. Prog Polym Sci 23(8):1443–1484. https://doi.org/10.1016/S0079-6700(98)00008-2
19. Andriianova AN, Biglova YN, Mustafin AG (2020) Effect of structural factors on the physicochemical properties of functionalized polyanilines. RSC Adv 10:7468–7491. https://doi.org/10.1039/C9RA08644G
20. Sha R, Komori K, Badhulika S (2017) Graphene–polyaniline composite based ultra-sensitive electrochemical sensor for non-enzymatic detection of urea. Electrochim Acta 233:44–51. https://doi.org/10.1016/j.electacta.2017.03.043
21. Li S, Ma Y, Liu Y, Xin G, Wang M, Zhang Z, Liu Z (2019) Electrochemical sensor based on a three dimensional nanostructured $MoS_2$ nanosphere-PANI/reduced graphene oxide composite for simultaneous detection of ascorbic acid, dopamine, and uric acid. RSC Adv 9:2997–3003. https://doi.org/10.1039/C8RA09511F

22. Promphet N, Rattanarat P, Rangkupan R, Chailapakul O, Rodthongkum N (2015) An electrochemical sensor based on graphene/polyaniline/polystyrene nanoporous fibers modified electrode for simultaneous determination of lead and cadmium. Sens Actuators B Chem 207:526–534. https://doi.org/10.1016/j.snb.2014.10.126
23. Chen G, Zheng J (2021) Non-enzymatic electrochemical sensor for nitrite based on a graphene oxide–polyaniline–Au nanoparticles nanocomposite. Microchem J 164:106034. https://doi.org/10.1016/j.microc.2021.106034
24. Hummers WS, Offeman RE (1958) Preparation of graphitic oxide. J Am Chem Soc 80:1339. https://doi.org/10.1021/ja01539a017
25. Yazid SNAM, Isa IM, Bakar SA, Hashim N (2015) Facile, cost effective and green synthesis of graphene in alkaline aqueous solution. Int J Electrochem Sci 10:7977–7984. https://doi.org/10.1016/S1452-3981(23)11070-4
26. Prasutiyo YJ, Manaf A, Hafizah MAE (2020) Synthesis of polyaniline by chemical oxidative polymerization and characteristics of conductivity and reflection for various strong acid dopants. J Phys Conf Ser 1442(1):012003. https://doi.org/10.1088/1742-6596/1442/1/012003
27. Stejskal J, Gilbert RG (2002) Polyaniline. Preparation of a conducting polymer (IUPAC technical report). Pure Appl Chem 74:857–867. https://doi.org/10.1351/pac200274050857
28. Xia X, Yang G, Tian H, Cao F, Luo F, Dong D (2025) Development of a rapid sensor system for nitrate detection in water using enhanced Raman spectroscopy. RSC Adv 15:5728–5736. https://doi.org/10.1039/D4RA08516G
29. Mafamadi M, Etale A, Daramola MO (2024) Synthesis and characterization of graphene oxide functionalized with dicarboxylic acids. Mater Today Proc 105:201–208. https://doi.org/10.1016/j.matpr.2023.08.291
30. Faniyi IO, Fasakin O, Olofinjana B, Adekunle AS, Oluwasusi TV, Eleruja MA, Ajayi EOB (2019) The comparative analyses of reduced graphene oxide (RGO) prepared via green, mild and chemical approaches. SN Appl Sci 1:1181. https://doi.org/10.1007/s42452-019-1188-7
31. Dhawan SK, Singh N, Venkatachalam S (2001) Shielding behaviour of conducting polymer-coated fabrics in X-band, W-band and radio frequency range. Synth Met 125:389–393. https://doi.org/10.1016/S0379-6779(02)00079-6
32. Tomsik E, Kohut O, Ivanko I, Pikarek M, Bieloshapka I, Dallas P (2018) Assembly and interaction of polyaniline chains: impact on electro- and physical–chemical behavior. J Phys Chem C 122:8022–8030. https://doi.org/10.1021/acs.jpcc.8b01948
33. Li H, Zhang Y, Feng K, Wei C (2023) Fabrication of graphene-assisted voltammetry platform for the detection of nitrate ions in PM2.5. Carbon Lett 33:2143–2152. https://doi.org/10.1007/s42823-023-00585-1
34. Abbas S, Yasmeen G, Manzoor S, Manzoor S, Hussain D, Yousaf A, Ashiq MN (2021) Synergistic effect of reduced graphene oxide layers wrapped in polyaniline sheets to porous blades for boosted oxygen evolution reaction. J Taibah Univ Sci 15:960–970. https://doi.org/10.1080/16583655.2021.2013650
35. Wang Y, Wang Y, Wang Y, Liu J (2023) Facial preparation of covalent modified reduced graphene oxide/polyaniline composite and its stable-enhanced electrochemical performance. Heliyon 9(1):e13002. https://doi.org/10.1016/j.heliyon.2023.e13002
36. Li J, Zhang J, Wei Y (2018) Electrochemical properties of polyaniline/graphene composites as electrode materials: influence of scan rate on redox behavior. Synth Met 244:36–44. https://doi.org/10.1063/5.0016905
37. Xu H, Ma Y, Chen J, Zhang WX, Yang J (2022) Electrocatalytic reduction of nitrate–a step towards a sustainable nitrogen cycle. Chem Soc Rev 51(7):2710–2758. https://doi.org/10.1039/D1CS00857A
38. Sapurina I, Stejskal J (2010) The mechanism of the oxidative polymerization of aniline and the formation of supramolecular polyaniline structures. Polym Int 59:1298–1325. https://doi.org/10.1002/pi.2476
39. Garcia-Segura S, Lanzarini-Lopes M, Hristovski K, Westerhoff P (2018) Electrocatalytic reduction of nitrate: fundamentals to full-scale water treatment applications. Appl Catal B Environ 236:546–568. https://doi.org/10.1016/j.apcatb.2018.05.041
40. Wei S, Xiao D, Li Y, Bian C (2024) Nitrate sensor with a wide detection range and high stability based on a Cu-modified boron-doped diamond electrode. Micromachines 15:487. https://doi.org/10.3390/mi15040487
41. Katsounaros I, Kyriacou G (2007) Influence of the concentration and the nature of the supporting electrolyte on the electrochemical reduction of nitrate on Tin cathode. Electrochim Acta 52:6412–6420. https://doi.org/10.1016/j.electacta.2007.04.050
42. Mirceski V, Komorsky-Lovric S, Lovric M (2007) Square-wave voltammetry: theory and application. Springer, Berlin Heidelberg
43. Teófilo RF, Reis EL, Reis C, da Silva GA, Kubota LT (2006) Use of factorial design for optimization of square-wave voltammetry parameters in glyphosate determination. J Braz Chem Soc 17:773–781. https://doi.org/10.1590/S0103-50532004000600013
44. Umar MF, Nasar A (2018) Reduced graphene oxide/polypyrrole/nitrate reductase deposited glassy carbon electrode (GCE/RGO/PPy/NR): biosensor for the detection of nitrate in wastewater. Appl Water Sci 8:211. https://doi.org/10.1007/s13201-018-0860-1
45. Adeloju SB, Sohail M (2011) Polypyrrole-based bilayer nitrate amperometric biosensor with an integrated permselective poly-ortho-phenylenediamine layer for exclusion of inorganic interferences. Biosens Bioelectron 26:4270–4275. https://doi.org/10.1016/j.bios.2011.04.002
46. Kosa SA, Khan AN, Ahmed S, Aslam M, Bawazir WA, Hameed A, Soomro MT (2022) Strategic electrochemical determination of nitrate over polyaniline/multi-walled carbon nanotubes–gum arabic architecture. Nanomaterials 12(19):3542. https://doi.org/10.3390/nano12193542
47. Kim MY, Lee JW, Lee JY, Myung NV, Kwon SH, Lee KH (2021) Highly stable potentiometric sensor with reduced graphene oxide aerogel as a solid contact for detection of nitrate and calcium ions. J Electroanal Chem 897:115553. https://doi.org/10.1016/j.jelechem.2021.115553
48. Gokhale AA, Lu J, Weerasiri RR, Yu J, Lee I (2015) Amperometric detection and quantification of nitrate ions using a highly sensitive nanostructured membrane electrocodeposited biosensor array. Electroanalysis 27:1127–1137. https://doi.org/10.1002/elan.201400547
49. Essousi H, Barhoumi H, Bibani M, Ktari N, Wendler F, Al-Hamry A, Kanoun O (2019) Ion-imprinted electrochemical sensor based on copper nanoparticles-polyaniline matrix for nitrate detection. J Sens 2019:4257125. https://doi.org/10.1155/2019/4257125
50. Ben Messaoud N, dos Santos MB, Espiña B, Queirós RB (2024) Development of electrochemical sensors based on silver nanoparticles electrodeposited on gold screen-printed electrodes: application to nitrate trace analysis in water. J Sens Sens Syst 13(1):135–145. https://doi.org/10.5194/jsss-13-135-2024

51. Di Masi S, Pennetta A, Guerreiro A, Canfarotta F, De Benedetto GE, Malitesta C (2020) Sensor based on electrosynthesised imprinted polymeric film for rapid and trace detection of copper (II) ions. Sens Actuators B Chem 307:127648. https://doi.org/10.1016/j.snb.2019.127648